RSC Advances

PAPER

View Article Online
View Journal | View Issue

Cite this: *RSC Adv.*, 2026, **16**, 22659

Functionalized bacteria used as adsorbents for uranium extraction from seawater

Xiaolei Chen, †[a] Jinzhao Tong,†[a] Xinqi Liang,[a] Zhan Li, [ab] Longlong Tian[ab] and Wangsuo Wu *[ab]

Selective extraction of uranium from seawater remains challenging due to its ultra-low concentration and the presence of competing ions. In this study, an engineered bacterial biosorbent (BDU09) was constructed by displaying the uranium-binding protein U09 on the outer membrane of *Escherichia coli* EcN 1917 *via* the Lpp-OmpA surface display system. To enhance mechanical stability and enable practical application, BDU09 cells were encapsulated within polyethylene glycol diacrylate (PEGDA), forming structurally stable microbial beads with high selectivity toward U(VI). Batch adsorption experiments demonstrated that both BDU09 and the corresponding microbial beads exhibited selective U(VI) uptake in the presence of competing ions, driven by specific coordination interactions between U(VI) and surface functional groups. The microbial beads maintained favorable selectivity and structural integrity in uranium-spiked simulated seawater as well as natural seawater. Continuous fixed-bed column experiments further confirmed effective U(VI) separation, with breakthrough behavior significantly influenced by initial concentration, bed height, and flow rate. The adsorption process was well described by the Yoon–Nelson model, and high-purity U(VI) recovery was achieved in simulated seawater. This work translates protein-level binding specificity into a mechanically robust and scalable biosorption platform, offering a promising strategy for uranium extraction from seawater.

Received 20th February 2026
Accepted 24th April 2026

DOI: 10.1039/d6ra01486k

rsc.li/rsc-advances

1 Introduction

With the continuous growth of global energy demand, nuclear energy has attracted considerable attention due to its high energy density and low carbon emissions. Uranium, primarily present as U(VI) and U(IV) in natural environments, is a critical resource for nuclear energy systems. At present, uranium resources are mainly obtained from terrestrial uranium ores, which are unevenly distributed and limited in reserve.[1,2] In contrast, seawater contains approximately 4.5 billion tons of uranium, nearly 1000 times that of terrestrial reserves, representing a potentially sustainable long-term resource for nuclear fuel supply.[3,4] However, uranium extraction from seawater remains challenging because of its extremely low concentration ($\sim$3.3 μg L^{-1}), its predominant existence as stable $Ca_2[UO_2(CO_3)_3]$ complexes, and the presence of abundant competing ions.[5–7]

Various strategies have been explored for uranium recovery from seawater, including membrane separation,[8,9] ion exchange,[10] electrochemical methods,[11] and adsorption techniques.[12,13] Among these, adsorption is considered one of the most promising approaches due to its operational simplicity, low energy consumption, and relatively low cost.[13] A wide range of adsorbent materials have been developed, such as carbon-based materials, metal–organic frameworks (MOFs), covalent organic frameworks (COFs), biopolymers, and amidoxime-functionalized materials.[14] For instance, Chang *et al.*[15] constructed a three-dimensional composite adsorbent composed of graphene oxide, ZIF-8, and sodium alginate with high uranium adsorption capacity, while Wei *et al.*[16] reported rapid U(VI) removal using glyphosate-modified MIL-101(Cr). Nevertheless, most synthetic adsorbents rely primarily on non-specific coordination interactions, often involving relatively complex synthesis procedures and high material costs, and may face challenges in long-term stability and environmental compatibility under complex marine conditions.[17] Therefore, developing selective, environmentally compatible, and efficient adsorption systems remains highly desirable.

Biomass-derived adsorbents, including bacteria,[18] proteins,[19] fibers,[20] chitin,[21] lignin,[22,23] and chitosan,[24] have attracted increasing interest owing to their renewability, biocompatibility, and abundance of functional groups. Compared with conventional synthetic materials, engineered microbial systems allow precise genetic control over surface functional groups and binding specificity. Recent studies have demonstrated the potential of engineered microorganisms for uranium and other

[a]*School of Nuclear Science and Technology, Lanzhou University, Tianshui South Road 222, Lanzhou 730000, China. E-mail: wuws@lzu.edu.cn*

[b]*Frontiers Science Center for Rare Isotopes, Lanzhou University, Tianshui South Road 222, Lanzhou 730000, China*

† These authors contributed equally to this work.

metal ions separation. Yuan *et al.*[18] isolated a *Bacillus* strain capable of uranium immobilization; Wang *et al.*[19] developed SUP chimeric protein fibers with enhanced mechanical strength for uranium enrichment from natural seawater; and Brewer *et al.*[25] achieved selective adsorption of rare earth elements using engineered *E. coli*. These findings suggest that rationally designed surface-displayed functional proteins can enable selective enrichment of target radionuclides.

The Lpp-OmpA system is a well-established outer membrane anchoring and surface display platform in Gram-negative bacteria, enabling stable presentation of heterologous proteins on the cell surface through coordinated interactions between lipoprotein signal peptides and β-barrel membrane structures.[26,27] EcN 1917, derived from the probiotic strain *Escherichia coli* Nissle 1917, possesses a well-characterized biosafety background and stable outer membrane architecture.[28] The U09 protein, originating from the archaeon *Methanobacterium thermoautotrophicum*, has been rationally engineered to exhibit high affinity toward UO_2^{2+} ions.[29] In this context, surface display of U09 provides a promising strategy to construct selective biosorbents. Accordingly, a novel engineered biosorbent (BDU09) was constructed in this study by expressing U09 on the outer membrane of EcN 1917 *via* the Lpp-OmpA display system.

Despite the promising selectivity of microbial and protein-based adsorption systems, their practical application is often limited by insufficient mechanical stability and poor adaptability to continuous-flow processes, which may result in structural collapse or column blockage. To address these limitations, BDU09 cells were encapsulated within polyethylene glycol diacrylate (PEGDA) microbial beads, enhancing mechanical strength while preventing clogging during continuous operation. The resulting microbial beads integrate protein-level binding specificity with polymer-based structural stability, enabling selective U(VI) adsorption and column separation. Furthermore, by replacing the surface-displayed functional proteins, this modular platform may be extended to the tailored separation of other radionuclides, providing new perspectives for uranium extraction from seawater and radioactive metal recovery.

2 Materials and methods

2.1 Materials

Luria–Bertani (LB) medium and L-arabinose were purchased from Solarbio (Beijing, China). Ampicillin was obtained from Servicebio (Hubei, China). Uranyl nitrate hexahydrate ($UO_2(NO_3)_2 \cdot 6H_2O$, purity ≥ 99.0%) was supplied by Chu Shengwei Chemical Co., Ltd (Hubei, China). Poly(ethylene glycol) diacrylate (PEGDA, Mn = 575) and 2-(*N*-morpholino)ethanesulfonic acid (MES) were purchased from Macklin (Shanghai, China). Ethyl (2,4,6-trimethylbenzoyl) phenylphosphinate (TPO-L) and piperazine-1,4-bis(ethanesulfonic acid) (PIPES) were obtained from Aladdin (Shanghai, China). Polydimethylsiloxane oil (PDMS oil, 10 cSt) was purchased from D&B (Shanghai, China). Triton X-45 was obtained from Merck (Germany). All chemicals were of analytical grade and used without further purification. Ultrapure water (18.2 MΩ cm) was used throughout all experiments.

2.2 Bacterial culture and preparation

The *Escherichia coli* EcN 1917 strain was kindly provided by Prof. Zhuang Liu (Soochow University, China). The construction and transformation of the Lpp-OmpA-Linker-U09-pBAD plasmid are described in SI 1 and Fig. S1. Western blot analysis was performed to qualitatively confirm the expression of U09. A flexible Gly-Ser-rich linker ($(GGGS)_3$) was introduced between the membrane anchor and U09 to reduce steric hindrance, improve conformational flexibility, and facilitate proper folding and surface exposure of the functional protein. The sequence of the fusion protein, including the linker region, is provided in the SI 2.

EcN 1917 cells harboring the Lpp-OmpA-Linker-U09-pBAD plasmid were cultured in LB medium containing 100 μg mL^{-1} ampicillin at 37 °C with shaking at 200 rpm. When the cells reached the logarithmic growth phase, L-arabinose was added to a final concentration of 0.2% (w/v) to induce U09 expression, followed by incubation at 25 °C overnight. Protein expression was verified by western blot analysis (Fig. 1a). Cells were subsequently harvested by centrifugation, washed once with 5 mM MES buffer (pH 6.0), and resuspended in the same buffer. The cell density was adjusted to approximately 1×10^{11} CFU per mL based on OD_{600} measurements calibrated by plate counting. The bacterial suspension was stored at 4 °C prior to use.

2.3 Preparation of microbial beads

Microbial beads were prepared through an emulsion photopolymerization process. Briefly, TPO-L photoinitiator (1 wt%) was first dissolved in PEGDA (Mn = 575, 99 wt%), and the resulting mixture was combined with the bacterial suspension at a volume ratio of 1 : 3 to form the aqueous phase, following the method reported by Brewer *et al.*.[30] The oil phase consisted of Triton X-45 (1 wt%) dissolved in PDMS oil (10 cSt, 99 wt%).

The aqueous phase was then added to the oil phase at a volume ratio of 1 : 7 and vortexed for approximately 15 s until a visually homogeneous emulsion was formed. The relatively high oil-phase fraction was chosen to stabilize the water-in-oil emulsion and prevent droplet coalescence, which is consistent with previous report,[30] thereby enabling the formation of uniform microbial beads. The emulsion was subsequently exposed to 365 nm UV irradiation (4 W cm^{-2}) for 60 s to initiate polymerization, resulting in the formation of PEGDA microbial beads encapsulating engineered bacteria.

After polymerization, the beads were collected by filtration through a 700-mesh nylon filter and washed ten times with physiological saline to remove residual oil and unreacted components. The final products were stored in 10 mM PIPES buffer (pH 7.0) at 4 °C prior to use. A schematic illustration of microbial beads preparation is shown in Fig. S2.

2.4 Batch adsorption and desorption experiments

2.4.1 Pretreatment of microbial beads and water content determination. Microbial beads stored in PIPES buffer were

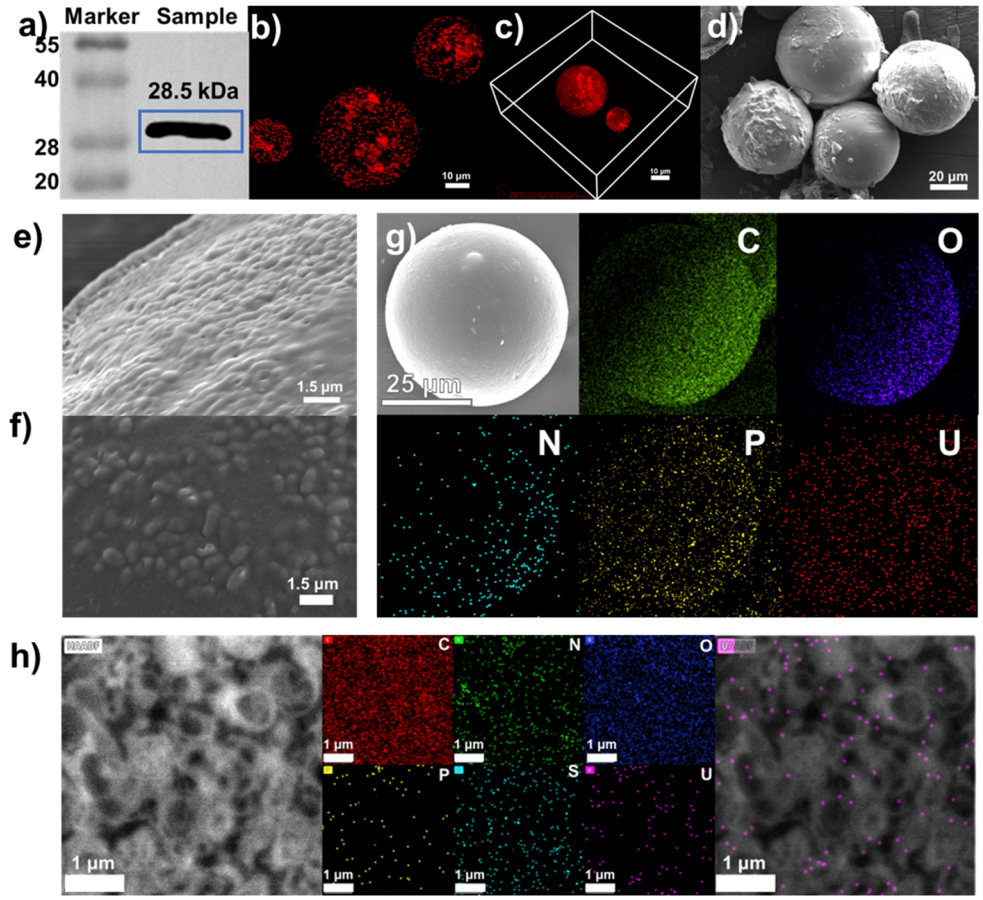

Fig. 1 Construction and structural characterization of engineered bacteria-encapsulated microbial beads. (a) Western blot analysis confirming successful expression of the target protein in engineered bacteria; (b) two-dimensional confocal laser scanning microscopy (CLSM) image of PI-stained bacteria within the microbial beads; (c) three-dimensional CLSM Z-stack reconstruction showing the spatial distribution of PI-stained bacteria inside the microbial beads; (d–f) scanning electron microscopy (SEM) images at different magnifications, showing the surface morphology of the microbial beads and associated bacterial distribution; (g) SEM-EDS elemental mapping images showing the spatial distribution of C, O, N, P, and U elements in the microbial beads after U(VI) adsorption; (h) transmission electron microscopy (TEM) image of an ultrathin section (~70 nm) of the microbial beads. Corresponding TEM-EDS elemental maps of C, N, O, P, S, and U from the same region are also shown, together with an overlay of the bright-field TEM image and the U elemental map.

filtered through a 700-mesh nylon filter and washed with 5 mM MES buffer (pH 6.0) to remove residual solution prior to weighing. A portion of the samples was freeze-dried at −60 °C under a vacuum of approximately 20 Pa for 72 h until constant weight was achieved. The water content was determined by comparing the mass before and after freeze-drying and was found to be 73.05 ± 0.13%. All adsorption capacities reported in this study were calculated based on dry weight.

2.4.2 Batch adsorption experiments. Batch adsorption experiments were conducted by varying parameters including initial U(VI) concentration, adsorbent dosage, solution pH, $NaNO_3$ concentration, temperature, and contact time to evaluate their effects on adsorption behavior. For isotherm studies, the initial U(VI) concentration ranged from 8 to 40 mg L^{-1}. All experiments were performed in a thermostatic shaker at 200 rpm.

After adsorption, the suspension was filtered through a 0.22 μm membrane to separate solid and liquid phases. The filtrate was acidified with nitric acid, and the residual U(VI) concentration was determined using inductively coupled plasma optical emission spectrometry (ICP-OES).

2.4.3 Adsorption–desorption cycling experiments. After reaching adsorption equilibrium, microbial beads were separated by filtration, washed three times with ultrapure water, and dried at room temperature to constant weight. The beads were then transferred into 0.1 mol L^{-1} sodium citrate solution and shaken until desorption equilibrium was achieved. The desorption solution was filtered through a 0.22 μm membrane, acidified, and analyzed by ICP-OES.

The desorbed beads were washed with ultrapure water, dried, and reused for subsequent adsorption cycles. The adsorption–desorption process was repeated for five cycles to evaluate reusability.

2.5 Dynamic column separation experiments

A fixed volume of wet microbial beads was wet-packed into a glass chromatography column (Φ4.0 mm × H80 mm), and

experiments were conducted at room temperature. The packed microbial beads in the column corresponded to approximately 0.0656 g (wet weight) for a 10 mm bed height and 0.1314 g (wet weight) for a 20 mm bed height. Based on a measured water content of ~73%, the corresponding dry weights were approximately 0.0177 g and 0.0355 g, respectively. All dynamic adsorption capacities (Q_t) were calculated based on dry weight. Breakthrough experiments were performed by varying initial U(VI) concentration, flow rate, and bed height to evaluate the effects of operational parameters on dynamic adsorption behavior.

For simulated seawater experiments, 10 mL of spiked simulated seawater was introduced into the column. The concentrations of major ions are listed in Table S2, and the initial U(VI) concentration was 14.85 mg L^{-1} (11.95 mg L^{-1} for spiked natural seawater). The column was then flushed with 15 mL of water and eluted using 15 mL of 0.1 mol L^{-1} sodium citrate solution. Effluents were collected automatically in 2 mL fractions, and subsequently acidified with nitric acid for ICP-OES analysis to determine the concentrations of U(VI) and other coexisting metal ions.

After each experiment, microbial beads in the column were kept immersed in MES buffer for subsequent reuse.

2.6 Calculation methods

The adsorption ratio (R_a), adsorption capacity (q_e and q_t), and distribution coefficient (K_d) were calculated using the following equations:

$$R_a = \frac{c_0 - c_e}{c_0} \times 100\% \quad (1)$$

$$q_e = \frac{(c_0 - c_e)V}{m} \quad (2)$$

$$q_t = \frac{(c_0 - c_t)V}{m} \quad (3)$$

$$K_d = \frac{c_0 - c_e}{c_e} \times \frac{V}{m} = \frac{q_e}{c_e} \quad (4)$$

where c_0, c_t, and c_e (mg L^{-1}) represent the initial concentration, concentration at time t, and equilibrium concentration, respectively; q_e and q_t (mg g^{-1}) denote equilibrium adsorption capacity and adsorption capacity at time t; m (mg) is the dry weight of adsorbent; V (mL) is the solution volume; R_a is the adsorption ratio (%); and K_d is the distribution coefficient (L g^{-1}).

3 Results and discussion

3.1 Characterization of microbial beads

3.1.1 Verification of protein expression and microbial beads construction. To verify the successful construction of the engineered bacteria and their incorporation into PEGDA microbial beads, protein expression was first characterized. As shown in Fig. 1a, a clear band appeared at approximately 28 kDa in the western blot analysis, consistent with the theoretical molecular weight of the target protein (28.5 kDa), confirming successful expression of the target protein in the engineered bacteria. The internal structure of the bacteria-loaded microbial beads was subsequently examined using confocal laser scanning microscopy (CLSM). As shown in Fig. 1b, PI-stained confocal images of microbial beads with three different sizes exhibit strong fluorescence signals throughout the beads, indicating successful encapsulation of bacteria within the microbial beads. Further three-dimensional Z-stack reconstruction (Fig. 1c) revealed a relatively uniform spatial distribution of bacteria within microbial beads of different sizes, without noticeable aggregation or void regions, suggesting good structural homogeneity of the microbial beads. The surface morphology of the microbial beads was further characterized by scanning electron microscopy (SEM). As shown in Fig. 1d–f, low-magnification images (Fig. 1d) demonstrate that the microbial beads exhibit a regular spherical morphology. At higher magnification (Fig. 1e), densely distributed bacterial protrusions can be observed on the microbial bead surface. Local magnification (Fig. 1f) further shows bacteria attached with different orientations and partially protruding from the surface, indicating that bacteria are not only uniformly distributed within the microbial beads but also form a continuous coverage on the surface.

Together, these results confirm successful protein expression, effective bacterial encapsulation, and structural integrity of the PEGDA-based microbial beads.

3.1.2 Spatial distribution of uranium after adsorption. After U(VI) adsorption, SEM–EDS elemental analysis was performed (Fig. 1g). The results show uniform distributions of C, N, O, and P elements across the microbial bead surface, with C and O signals dominating. Meanwhile, the U signal is also homogeneously distributed, indicating that U(VI) adsorption does not lead to significant localized enrichment or precipitation at the microbial bead scale. To further resolve the spatial distribution of uranium at higher resolution, ultrathin sections (~70 nm) were prepared for TEM–EDS analysis (Fig. 1h). Bacterial structures are clearly identifiable in the TEM bright-field images, while elemental mapping shows uniform distributions of C, N, O, P, S, and U within the observed region. Overlaying the U elemental map with the bright-field image reveals that uranium signals are mainly localized around the bacterial periphery, suggesting that U(VI) is primarily associated with regions near the cell membrane, consistent with the membrane localization of the expressed target protein. These observations reflect a multi-scale distribution behavior, where uranium appears uniformly distributed at the bead scale while being preferentially associated with bacterial interfaces at higher resolution, indicating that adsorption primarily occurs on bacterial surfaces that are homogeneously dispersed throughout the microbial beads.

3.1.3 Functional group interactions and chemical-state evolution (FTIR and XPS). Fourier transform infrared spectroscopy (FTIR) was employed to investigate changes in surface functional groups of bacteria before and after U(VI) adsorption (Fig. 2a). Both samples exhibit a broad and intense absorption band above 3000 cm^{-1}, commonly attributed to the stretching vibrations of hydroxyl (–OH) and amino (–NH) groups

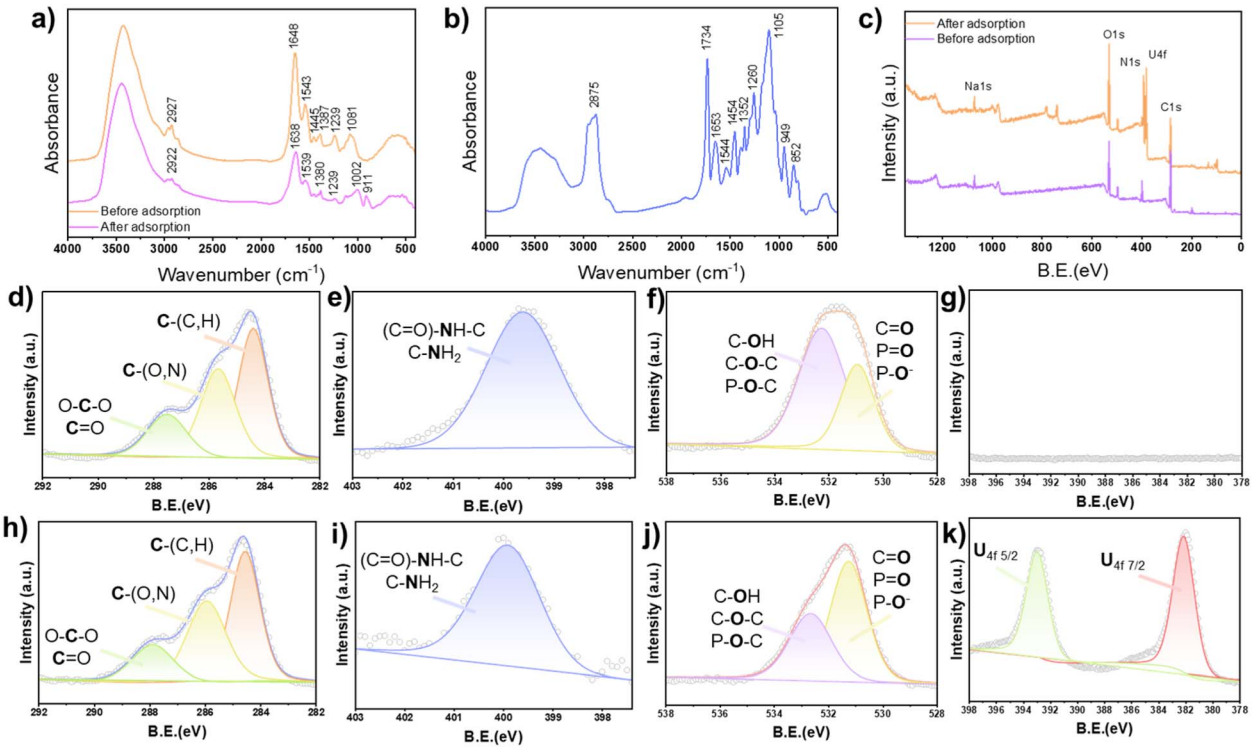

Fig. 2 Spectroscopic characterization of bacteria before and after U(VI) adsorption, and of PEGDA microbial beads; (a) FTIR spectrum of bacteria before and after U(VI) adsorption; (b) FTIR spectrum of pristine PEGDA microbial beads; (c) XPS survey spectra of bacteria before and after U(VI) adsorption; (d–g) High-resolution XPS spectra of C 1s, N 1s, O 1s, and U 4f regions of bacteria before U(VI) adsorption; (h–k) High-resolution XPS spectra of C 1s, N 1s, O 1s, and U 4f regions of bacteria after U(VI) adsorption.

originating from polysaccharides, proteins, and adsorbed water on the bacterial surface.[31] The overall shape and intensity of this band remain largely unchanged after adsorption, indicating that hydrophilic functional groups are preserved during the adsorption process. The absorption peak near 2922 cm^{-1} corresponds to aliphatic $-CH_2/-CH_3$ stretching vibrations associated with membrane lipids,[31,32] showing negligible changes after adsorption and suggesting that the lipid backbone structure remains intact. In the mid-wavenumber region, characteristic amide I (C=O stretching) and amide II (N–H bending coupled with C–N stretching) bands appear at 1648 cm^{-1} and 1543 cm^{-1}, respectively.[33] After U(VI) adsorption, these peaks slightly shift to 1638 cm^{-1} and 1539 cm^{-1}, indicating changes in the local chemical environment of carbonyl and amino groups, possibly due to interactions between uranyl ions and oxygen- or nitrogen-containing functional groups. In the fingerprint region (1500–1000 cm^{-1}), multiple weak bands associated with C–O, P–O, and C–O–C vibrations are observed,[34] and partial variations in peak shape and intensity after adsorption suggest rearrangement of oxygen-containing functional groups during uranyl binding. Notably, a new band at 911 cm^{-1} can be attributed to the characteristic O=U=O stretching vibration of uranyl species. Compared with typical values reported for aqueous uranyl species, this band may reflect a shift in vibrational frequency due to coordination interactions with surface functional groups, providing spectroscopic evidence for U(VI) adsorption. In the low-wavenumber region (500–600 cm^{-1}), a broad weak band is observed both before and after adsorption,[35] which is discussed qualitatively due to its low resolution. FTIR analysis of PEGDA microbial beads (Fig. 2b) shows characteristic absorption peaks at 1734 cm^{-1} corresponding to ester C=O stretching, at 1653 cm^{-1} related to C=C bonds, and at 1105 cm^{-1} assigned to C–O–C stretching vibrations, confirming the successful formation of the PEGDA crosslinked polymer network.[36,37] These results indicate that PEGDA mainly provides structural support, while functional group variations associated with adsorption originate predominantly from bacterial components.

X-ray photoelectron spectroscopy (XPS) was further conducted to analyze changes in surface elemental composition and chemical states before and after adsorption (Fig. 2c). The survey spectrum of the pristine sample shows dominant C 1s, N 1s, and O 1s signals, corresponding to organic and nitrogen-containing functional groups on the bacterial surface. After adsorption, distinct uranium-related peaks appear while C, N, and O signals remain present, confirming successful immobilization of uranyl species on the surface. High-resolution spectra of C 1s, N 1s, O 1s, and U 4f (Fig. 2d–k) were further analyzed within the XPS probing depth (~3–5 nm). The C 1s spectra (Fig. 2d and h) can be deconvoluted into three components at approximately 284.4 eV, 285.6 eV, and 287.5 eV, assigned to C–C/C–H, C–O/C–N, and O–C–O/C=O bonds, respectively.[38] No obvious chemical shift or significant change in relative distribution is observed after adsorption, indicating that the organic framework remains chemically stable. The N 1s spectra (Fig. 2e and i) show a dominant peak centered at

approximately 399.6 eV, attributed to amine or amide nitrogen species.[39,40] After adsorption, slight baseline elevation is observed, mainly due to the adjacent strong U 4f signal at higher binding energy. The O 1s spectra (Fig. 2f and j) can be fitted into two components. Before adsorption, peaks appear at approximately 530.9 eV and 532.2 eV, while after adsorption they shift to 531.2 eV and 532.6 eV. The lower binding energy component is typically associated with C═O, P═O, or P–O groups, whereas the higher binding energy component corresponds to C–OH, C–O–C, and P–O–C species.[41] Notably, the relative intensity of the double-bonded oxygen component increases after adsorption, accompanied by positive shifts of 0.32 eV and 0.42 eV, respectively, indicating the involvement of oxygen-containing functional groups in uranyl coordination.[42] The positive shift suggests a decrease in local electron density around oxygen atoms upon coordination with uranyl ions, consistent with electron donation from oxygen ligands to the uranium center. This observation agrees with the reported binding mode of the U09 protein, in which carboxyl groups from Glu8, Glu12, and Glu35, together with a coordinated water molecule, interact with the equatorial plane of the uranyl ion (Fig. S3).[29] In the U 4f region, two new peaks appear at approximately 382.16 eV (U $4f_{7/2}$) and 392.96 eV (U $4f_{5/2}$) after adsorption, while no uranium-related signal is detected in the pristine sample (Fig. 2g and k), directly confirming successful enrichment of uranyl species on the material surface.[43] The relatively sharp peak shape suggests that uranium exists in a relatively uniform chemical state.

3.2 Effect of contact time, solid–liquid ratio, and initial acidity

The adsorption behavior of metal ions on adsorbents is influenced by both the physicochemical properties of the adsorbent surface and solution conditions, including metal speciation, concentration, solution acidity, and medium composition. Fig. 3a shows the variation of adsorption percentage with contact time under conditions of [U(VI)] = 25 ppm, T = 25 °C, pH = 5, and m V^{-1} = 0.4 mg mL^{-1}. Rapid adsorption occurs during the initial stage, reaching 37% within 3 h. After 15 h, the adsorption percentage reaches 40%, corresponding to an adsorption capacity of 25 mg g^{-1}, and subsequently remains stable. This behavior indicates that adsorption initially occurs on readily accessible surface sites, followed by a slower stage that may be associated with mass transfer resistance within the PEG network until adsorption–desorption equilibrium is achieved. Therefore, an equilibrium time of 24 h was adopted for subsequent experiments.

Adsorption kinetics analysis was conducted to further investigate the adsorption behavior of U(VI), including possible contributions from external diffusion, internal diffusion, and surface interactions. The pseudo-first-order (eqn (5)) and pseudo-second-order (eqn (6)) kinetic models are commonly used to describe adsorption behavior of metal ions.[44] The pseudo-first-order model is generally associated with diffusion-related processes, whereas the pseudo-second-order model assumes that the adsorption rate is related to the availability of adsorption sites.

$$q_t = q_e \times \left(1 - e^{-k_1 t}\right) \quad (5)$$

$$q_t = \frac{k_2 t q_e^2}{1 + k_2 t q_e} \quad (6)$$

Fitting of the experimental data using eqn (5) and (6) produced the curves shown in Fig. 3b and c, with correlation coefficients (R^2) of 0.8826 and 0.9999, respectively. The results indicate that the pseudo-second-order model provides a better description of the adsorption behavior of U(VI), suggesting that the adsorption process is more closely related to the availability of active sites and surface interactions rather than being solely controlled by diffusion. The calculated equilibrium adsorption capacity (q_e = 26.18 mg g^{-1}) agrees well with the experimentally obtained value (25 mg g^{-1}) obtained under the same conditions ([U(VI)] = 25 ppm, pH = 5, T = 25 °C, m V^{-1} = 0.4 mg mL^{-1}).

The solid–liquid ratio (m V^{-1}) significantly influences the adsorption performance of U(VI). As shown in Fig. 3d, increasing the adsorbent dosage increases the adsorption percentage from 45% to 83%, while the adsorption capacity decreases from 18.4 mg g^{-1} to 12.8 mg g^{-1}. This behavior indicates that although more adsorption sites become available at higher dosages, incomplete utilization of active sites, together with possible site overlap and reduced concentration gradients, leads to a decrease in unit mass adsorption capacity.[16]

The effect of solution pH on adsorption percentage is shown in Fig. 3e, while Fig. 3f presents the calculated speciation distribution of U(VI) over pH 1–14 using Visual MINTEQ 3.1. The adsorption percentage increases from 18% to 90% as pH rises from 3 to 6, reaches a maximum at pH 6, and decreases at higher pH values, consistent with previous reports.[45–47] At pH < 5, U(VI) mainly exists as UO_2^{2+}, and competition between H^+ and adsorption sites results in relatively low adsorption efficiency.[45] When 5 < pH < 8, hydrolyzed uranyl species such as $(UO_2)_3(OH)_5^+$ and $(UO_2)_4(OH)_7^+$ gradually form, while deprotonation of surface functional groups enhances coordination interactions with U(VI), leading to improved adsorption performance. At pH > 8, negatively charged hydroxo complexes, including $(UO_2)_3(OH)_7^-$, $UO_2(OH)_3^-$, and $UO_2(OH)_4^{2-}$, become dominant. The presence of these species may lead to electrostatic repulsion between uranyl complexes and the adsorbent surface, resulting in decreased adsorption efficiency.[46] Therefore, adsorption of U(VI) on microbial surfaces is likely governed by the combined effects of coordination interactions between amino acid functional groups and uranyl ions together with electrostatic interactions.

3.3 Adsorption isotherm study

Adsorption isotherms were employed to describe the adsorption behavior of the adsorbent at different equilibrium concentrations. The Langmuir and Freundlich models are commonly used to analyze adsorption processes. The Langmuir model assumes monolayer adsorption on a homogeneous

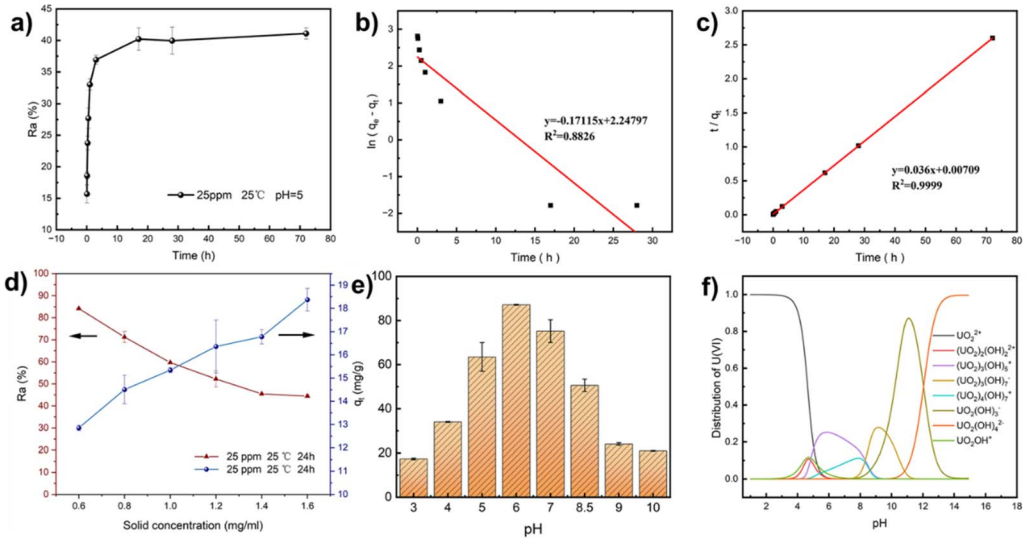

Fig. 3 (a) Effect of contact time on U(VI) adsorption by microbial beads, [UO_2^{2+}] = 25 ppm, T = 25 °C, pH = 5, m V^{-1} = 0.4 mg mL^{-1}; (b) Pseudo-first-order kinetic model fitting; (c) Pseudo-second-order kinetic model fitting; (d) effect of adsorbent dosage on U(VI) adsorption by microbial beads, [UO_2^{2+}] = 25 ppm, T = 25 °C, pH = 5, t = 24 h; (e) adsorption edges of U(VI) at different pH values on microbial beads, [UO_2^{2+}] = 25 ppm, T = 25 °C, t = 24 h, m V^{-1} = 0.1 mg mL^{-1}; (f) the relative species of U(VI) as a function of pH value (simulated using Visual MINTEQ v3.1).

surface with finite and identical active sites, whereas the Freundlich model is an empirical equation describing multi-layer adsorption on heterogeneous surfaces. The mathematical expressions of the Langmuir and Freundlich models are given in eqn (7) and (8), respectively:

$$\frac{C_e}{q_e} = \frac{1}{q_{max} K_L} + \frac{C_e}{q_{max}} \quad (7)$$

$$\ln q_e = \ln K_F + \left(\frac{1}{n}\right) \ln C_e \quad (8)$$

where K_L is the Langmuir constant, and K_F and n are Freundlich constants.

The Langmuir and Freundlich fitting results at 283, 298, and 323 K are presented in Fig. 4a and b, respectively. The equilibrium adsorption capacity of U(VI) increased with increasing temperature, indicating that elevated temperature favored the adsorption process. In addition, higher initial concentrations resulted in increased equilibrium adsorption capacities due to the enhanced concentration gradient between solution and adsorbent surface. The corresponding fitting parameters and correlation coefficients (R^2) are summarized in Table 1. Both K_F

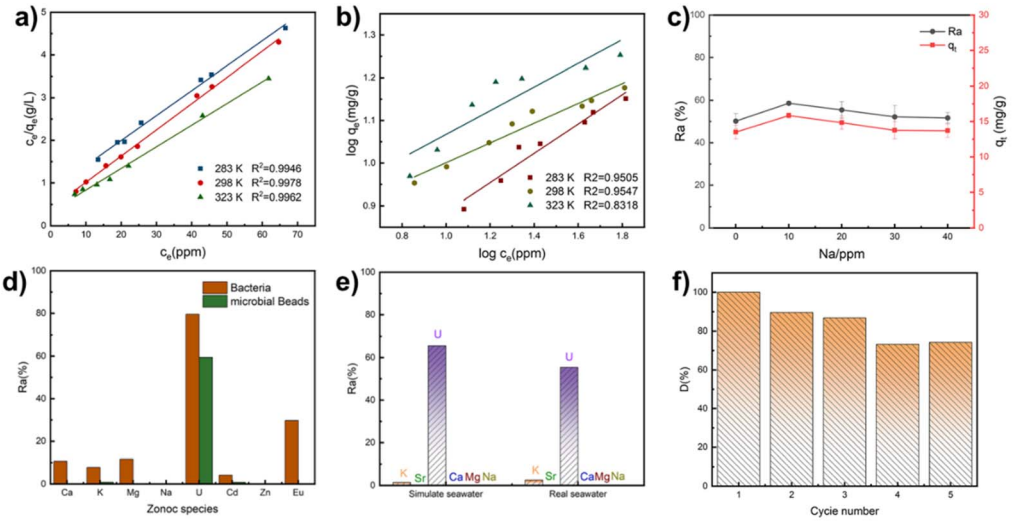

Fig. 4 (a) Linear fitting of the Langmuir isotherm at different temperatures; (b) Linear fitting of the Freundlich isotherm model at different temperatures; (c) effect of ionic strength on the adsorption percent and capacity of microbial beads; (d) effect of competitive cations on the adsorption of U(VI) by bacteria and microbial beads (cations: K^+, Na^+, Ca^{2+}, Mg^{2+}, Cd^{2+}, Zn^{2+}, Eu^{3+}; [M] = 1×10^{-4} mol L^{-1}, m V^{-1} = 1 mg mL^{-1}, pH = 5); (e) removal efficiency of microbial beads in spiked simulated seawater (left) and spiked natural seawater (right) (The concentration of cation can be seen in table S2). (f) Reusability of microbial beads in U(VI) adsorption.

Table 1 U(VI) sorption isotherms parameters of the models

Isotherm	Parameter	Temperature/K 283	298	323
Freundlich	$1/n$	0.3433	0.2317	0.2772
	K_F [(mg g^{-1})/(mg L^{-1})$^{1/n}$]	3.4866	5.8780	6.1700
	R^2	0.9505	0.9547	0.8318
Langmuir	K_L (L mg^{-1})	0.0706	0.1532	0.1560
	q_{max} (mg g^{-1})	17.11	16.26	19.69
	R^2	0.9946	0.9978	0.9962

and K_L increased with temperature, further suggesting that adsorption was thermodynamically favorable at higher temperatures. However, excessive temperature may affect the structural stability of the microbial beads. As shown in Fig. S4, high-temperature treatment or prolonged UV exposure resulted in decreased adsorption capacity, which may be attributed to structural alterations or partial denaturation of bacterial proteins.[47] Comparison of correlation coefficients indicates that the Langmuir model provided a better fit than the Freundlich model, with R^2 values closer to unity. This result suggests that U(VI) adsorption on the microbial beads predominantly follows monolayer adsorption behavior with relatively uniform active sites.

3.4 Effect of ionic strength and competing ions

The influence of ionic strength on U(VI) adsorption onto microbial beads is shown in Fig. 4c. Within the $NaNO_3$ concentration range of 0.1–40 ppm, the adsorption percentage remained between 50% and 60%, and the adsorption capacity was maintained at approximately 13–15 mg g^{-1}. These results indicate that variations in ionic strength exert only a minor influence on U(VI) adsorption. Therefore, the adsorption behavior suggests the involvement of inner-sphere surface complexation.[48] In the inner-sphere complexation model, adsorbed ions directly coordinate with surface functional groups without the involvement of intermediate water molecules, resulting in strong and specific chemical interactions. This interpretation is consistent with the post-adsorption characterization results. In contrast, outer-sphere complexation involves at least one water molecule between the adsorbate and surface functional groups, leading to nonspecific adsorption that is more sensitive to changes in ionic strength; elevated salt concentrations typically reduce adsorption capacity under such mechanisms.[49] The weak dependence on ionic strength observed here suggests that the microbial beads maintain stable adsorption performance under high-salinity and high-ionic-strength conditions, highlighting their potential for uranium extraction from seawater. However, further control experiments would be required to fully distinguish specific coordination from non-specific adsorption.

In addition to U(VI), seawater contains various competing metal cations, including K(I), Na(I), Mg(II), Ca(II), Zn(II), Cd(II), and Eu(III), which may compete for adsorption sites and influence selectivity. The adsorption percentages of different metal ions on BDU09 and microbial beads are presented in Fig. 4d. The microbial beads exhibited significantly higher adsorption toward U(VI), reaching 80% and 60%, respectively, while adsorption toward competing ions remained below 2%. In contrast, BDU09 showed higher adsorption toward impurity ions, with Eu(III) reaching up to 25% and other ions below 10%.

The separation factor between U(VI) and competing metal ions ($SF_{U/M}$) was calculated using eqn (9):

$$SF_{U/M} = \frac{K_d^U}{K_d^M} \quad (9)$$

As summarized in Table S1, the highest and lowest separation factors for BDU09 were 7.9×10^3 (U/Na) and 2.7 (U/Eu), respectively. For microbial beads, the highest separation factors reached 5.9×10^3 (U/Ca and U/Mg), while the lowest value was 67.3 (U/K). Although the adsorption capacities of microbial beads toward some metal ions were lower than those of BDU09, the substantially reduced adsorption toward competing ions resulted in enhanced overall separation selectivity.

3.5 Adsorption in spiked simulated seawater and natural seawater

Natural seawater contains not only abundant inorganic ions but also various organic substances and microorganisms,[16] all of which may influence adsorption performance. Therefore, evaluating adsorption behavior under seawater conditions is essential for practical applications. The adsorption performance of microbial beads was investigated in both spiked simulated seawater and spiked natural seawater, with compositions listed in Table S2. The results are shown in Fig. 4e.

In both systems, the adsorption of abundant competing divalent cations such as Mg^{2+} and Ca^{2+} remained very low, while U(VI) adsorption maintained good selectivity. The removal efficiency of U(VI) reached approximately 65% in simulated seawater and slightly decreased to 55% in natural seawater.

The reduced adsorption performance in seawater can be attributed to the complex ionic composition. The presence of high concentrations of CO_3^{2-} and Ca^{2+} promotes the formation of neutral complexes such as $Ca_2UO_2(CO_3)_3(aq)$,[50] rather than positively charged UO_2^{2+} or hydroxyl complexes. The formation of neutral species weakens electrostatic interactions between U(VI) and adsorption sites. Furthermore, organic matter and microorganisms present in natural seawater may further interfere with adsorption, leading to additional decreases in removal efficiency.

3.6 Desorption and reusability

Reusability is an important criterion for evaluating the industrial applicability of adsorbents. The adsorption–desorption cycling performance of microbial beads for U(VI) was therefore investigated. As shown in Fig. 4f, the desorption percentage as a function of cycle number was evaluated according to eqn (10), where m_{ad} represents the amount of U(VI) adsorbed per unit

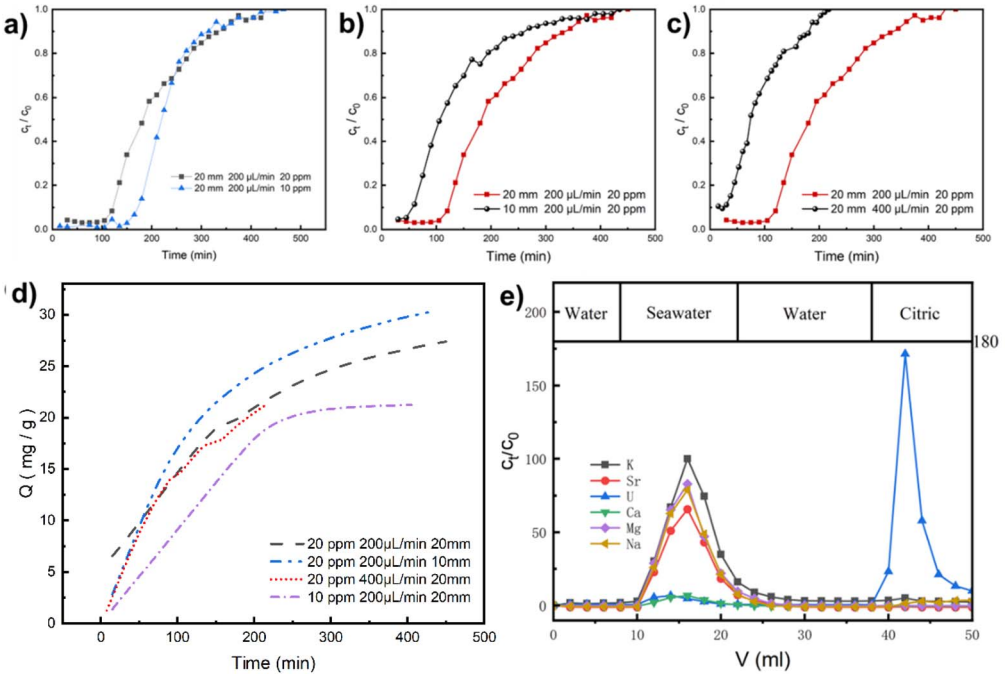

Fig. 5 (a) Breakthrough curves of U(VI) in the microbial beads column at different U(VI) concentrations; (b) breakthrough curves of U(VI) through microbial beads column at different column heights; (c) breakthrough curves of U(VI) through microbial beads column at different flow rates; (The experimental conditions shown in the figure are column height (mm), flow rate (μL min^{-1}), and U(VI) concentration (ppm)). (d) U(VI) adsorption capacity of microbial beads as a function of time under different experimental conditions; (e) Column separation of spiked simulated seawater through microbial beads column. pH = 5, room temperature, column diameter = 5 mm.

mass of adsorbent during adsorption and m_{de} represents the amount desorbed into solution during desorption.

$$D\% = \frac{m_{de}}{m_{ad}} \times 100\% \quad (10)$$

The initial desorption efficiency reached nearly 100%. Although a gradual decline in adsorption–desorption performance was observed with increasing cycle number, the desorption efficiency remained above 70% after five cycles, demonstrating good regeneration capability and structural stability of the microbial beads.

To evaluate the structural stability of microbial beads after repeated adsorption–desorption cycles, SEM images were obtained after five cycles (Fig. S5). Compared with the pristine microbial beads (Fig. 1e–f), the cycled beads exhibit a slightly roughened surface with the appearance of micro-scale irregularities. However, the overall spherical morphology and structural integrity are well preserved, with no obvious collapse or fragmentation observed. This result indicates that the PEGDA-based microbial beads maintain good structural stability during repeated adsorption–desorption processes, which is consistent with the retained adsorption performance.

3.7 Column separation experiments

The photo of the column setup is shown in Fig. S6. Breakthrough curves obtained under different initial U(VI) concentrations, column heights, and flow rates are presented in Fig. 5a–c. Here, C_0 and C_t represent the initial concentration and the concentration at time t, respectively, and the x-axis denotes the operating time after the U(VI) solution entered the column. The dynamic adsorption behavior of microbial beads under various operating conditions is summarized in Fig. 5d.

Table 2 Yoon–Nelson parameters for dynamic adsorption of U(VI) and Q_t on microbial beads at different experimental condition[a]

U(VI) concentration (ppm)	Flow rate (μL min^{-1})	Column height (mm)	K_{YN} (min^{-1})	τ (min)	τ_{exp} (min)	R^2	Q_t (mg g^{-1})
20	200	20	0.0201	197.29	182.58	0.9516	28.33
20	200	10	0.0112	119.64	106.38	0.9720	30.33
20	400	20	0.0298	82.04	73.91	0.9226	23.22
10	200	20	0.0340	224.24	219.87	0.9930	20.63

[a] τ: the time required to adsorb 50% of U(VI) according to model calculation; τ_{exp}: the time required to adsorb 50% of U(VI) according to the experiments; Q_t: the adsorption capacity of U(VI) by microbial beads.

The dynamic adsorption capacity (Q_t) was calculated according to eqn (11), where m and v represent the mass of microbial beads and flow rate, respectively:

$$Q_t = \frac{v\int_0^t (C_0 - C_t)\,dt}{m} \quad (11)$$

When flow rate and column height were kept constant, breakthrough curves obtained at initial U(VI) concentrations of 10 and 20 ppm are shown in Fig. 5a. Earlier breakthrough occurred at higher feed concentrations, indicating faster saturation of adsorption sites. The corresponding experimental breakthrough times (τ_{exp}, defined as the time when $C_t/C_0 = 0.5$) were 219.87 and 182.58 min, respectively (Table 2). Lower feed concentrations reduced the concentration gradient and mass transfer driving force, thereby prolonging breakthrough time but resulting in lower saturation capacity.[51] In this study, the column performance was primarily evaluated based on experimental breakthrough behavior, while the Yoon–Nelson model was further applied for quantitative analysis.

Under identical initial concentration and flow rate conditions, increasing column height from 10 to 20 mm increased τ_{exp} from 119.64 to 182.58 min and slightly decreased Q_t from 30.33 to 28.33 mg g^{-1} (dry weight basis). A higher column height provides more active sites and longer residence time, thereby improving overall adsorption performance.[52]

When initial concentration and column height were fixed, increasing the flow rate from 200 to 400 μL min^{-1} reduced τ_{exp} from 182.58 to 73.91 min and decreased the adsorption capacity from 28.33 to 23.22 mg g^{-1} (dry weight basis). Higher flow rates shorten solution residence time, limiting equilibrium between U(VI) and adsorption sites and leading to earlier breakthrough and reduced adsorption capacity.[53,54]

The experimental data were further fitted using the Yoon–Nelson model,[55] expressed in eqn (12):

$$\frac{C_t}{C_0} = \frac{1}{1 + \exp(K_{YN}(\tau - t))} \quad (12)$$

where K_{YN} is the rate constant associated with mass transfer and τ is the theoretical breakthrough time. The fitting results (Fig. S7a–d) show good agreement with experimental data, with deviations between calculated and experimental breakthrough times below 10% and correlation coefficients higher than 0.92, indicating that the Yoon–Nelson model adequately describes the dynamic adsorption behavior of U(VI) in the fixed-bed column.

As shown in Fig. 5d and Table 2, the adsorption capacity gradually increased with operating time and eventually approached saturation. Within the investigated conditions, lower column height resulted in higher adsorption capacity per unit mass, whereas lower initial concentration led to reduced adsorption capacity, and increased flow rate shortened the time required to reach saturation.

Column separation performance in spiked simulated seawater is shown in Fig. 5e (composition listed in Table S2). Coexisting divalent ions such as Ca^{2+}, Mg^{2+}, and Sr^{2+} were scarcely retained in the column, indicating weak interaction with the adsorbent. In contrast, monovalent ions (*e.g.*, Na^+ and K^+) were still detected in the eluent due to their high background concentrations. U(VI), however, was effectively adsorbed and selectively eluted using sodium citrate solution. Citrate forms stable complexes with U(VI), enabling its desorption from active sites. The calculated adsorption and desorption efficiencies of U(VI) were approximately 80% and 62%, respectively. Although U(VI) was effectively enriched during the elution stage, monovalent ions such as Na^+ and K^+ were still present due to their high background concentrations. In contrast, divalent ions (*e.g.*, Ca^{2+} and Mg^{2+}) showed negligible elution, indicating the selective recovery of U(VI).

4 Conclusion

In this study, an engineered biosorbent (BDU09) was constructed by displaying the U09 peptide on the surface of *Escherichia coli* EcN 1917 *via* the Lpp-OmpA system. Encapsulation with PEGDA produced structurally stable microbial beads with selective adsorption toward U(VI). The adsorption process followed the Langmuir model and exhibited favorable selectivity in multi-ion systems, including simulated and natural seawater. Fixed-bed column experiments confirmed effective dynamic separation of U(VI), and the breakthrough behavior was well described by the Yoon–Nelson model. These results demonstrate the potential of the engineered microbial beads for uranium recovery from seawater.

Author contributions

Xiaolei Chen: writing – original draft, data curation. Jinzhao Tong: data curation. Xinqi Liang: validation, investigation. Longlong Tian: resources. Zhan Li: writing – review & editing, supervision. Wangsuo Wu: resources, funding acquisition.

Conflicts of interest

The authors declare that they have no known competing financial interests or personal relationships that could have appeared to influence the work reported in this paper.

Data availability

All relevant data to support this research are given in the article.

Supplementary information (SI) is available. See DOI: https://doi.org/10.1039/d6ra01486k.

Acknowledgements

The authors gratefully acknowledge Prof. Zhuang Liu at Soochow University for generously providing the bacterial strains used in this study. We thank Ms. Ning Zhang at Electron Microscopy Center of Lanzhou University for assistance with the room-temperature ultramicrotome (Leica EM UC7).

References

1 T. P. Wang, Z. Q. Wu, W. Xiong, X. Z. Pan, X. Ye and X. G. Liu, The Impact of Uranium Resource Constraints on China's Nuclear Power Development, *Energies*, 2025, **18**(6), 1507, DOI: 10.3390/en18061507.

2 S. Gabriel, A. Baschwitz, G. Mathonnière, T. Eleouet and F. Fizaine, A critical assessment of global uranium resources, including uranium in phosphate rocks, and the possible impact of uranium shortages on nuclear power fleets, *Ann. Nucl. Energy*, 2013, **58**, 213–220, DOI: 10.1016/j.anucene.2013.03.010.

3 Y. C. Song, B. L. Deng, K. Wang, Y. J. Zhang, J. Gao and X. Q. Cheng, Highly-efficient adsorbent materials for uranium extraction from seawater, *J. Environ. Chem. Eng.*, 2024, **12**(5), 113967, DOI: 10.1016/j.jece.2024.113967.

4 C. Y. Cui, J. J. Wu, X. Y. Yu and S. T. Zhang, New Methodological Research Progress in Uranium Extraction from Seawater, *Chem. Res. Chin. Univ.*, 2025, **41**, 1557–1571, DOI: 10.1007/s40242-025-5241-3.

5 Y. Ding, Q. H. Liu, X. S. Shi, S. Wu, Z. Y. Feng, L. Zhu, C. X. Zhang, L. B. Yang, H. T. Wu and S. S. Chen, Enhanced photocatalytic extraction of the g-C3N4 NTs in situ co-grafted carbonyl and amide oxime groups for uranium from seawater, *Sep. Purif. Technol.*, 2026, **382**(1), 135587, DOI: 10.1016/j.seppur.2025.135587.

6 W. S. Zhang, M. Q. Wu, Y. Y. Xin, H. Z. Liu, F. W. Li and Y. Fa, Comparative analysis of seawater uranium extraction materials: Toward the development of bio-based and biomimetic materials, *Coord. Chem. Rev.*, 2025, **534**, 216589, DOI: 10.1016/j.ccr.2025.216589.

7 N. Shi, J. K. Wu, X. Y. Zhi, N. Li and Z. N. Wang, Amidoxime-functionalized cellulose nanofibers/MXene aerogel for electric field enhanced uranium extraction from seawater, *Chem. Eng. J.*, 2023, **476**, 146563, DOI: 10.1016/j.cej.2023.146563.

8 Z. Liu, H. H. Tan, Y. L. Shao, G. L. Nie, Z. W. Hou, P. P. Yang, S. W. Li and C. T. Liu, Membrane-based adsorbent materials for uranium extraction from seawater: recent progress and future prospects, *Nanoscale*, 2025, **17**, 9764–9785, DOI: 10.1039/d4nr04603j.

9 Y. Yu, J. Y. Liu, Q. Liu, Y. D. Xue, R. R. Chen, J. Yu, J. H. Zhu and J. Wang, High-Performance Polyamidoxime Porous Membrane Prepared by the In Situ Modification/Nonsolvent-Induced Phase Separation Strategy for Uranium Extraction from Seawater, *ACS Appl. Mater. Interfaces*, 2024, **16**, 49778–49789, DOI: 10.1021/acsami.4c09875.

10 J. Q. Li, L. L. Gong, X. F. Feng, L. Zhang, H. Q. Wu, C. S. Yan, Y. Y. Xiong, H. Y. Gao and F. Luo, Direct extraction of U(VI) from alkaline solution and seawater via anion exchange by metal-organic framework, *Chem. Eng. J.*, 2017, **316**, 154–159, DOI: 10.1016/j.cej.2017.01.046.

11 Y. J. Wang, Y. Cao, X. Wang, S. Y. Wang and Y. Y. Wang, Research progress on low-energy and high-efficiency electrochemical seawater uranium extraction systems, *Sci. China Chem.*, 2025, **68**, 6328–6338, DOI: 10.1007/s11426-025-3148-4.

12 Y. H. Yang, F. F. Lan, L. Shi, X. H. Li and Y. Yang, Uranium extraction from seawater: Progress and challenges, *J. Environ. Chem. Eng.*, 2026, **14**(1), 120945, DOI: 10.1016/j.jece.2025.120945.

13 H. Y. Zhou, F. Yu, M. H. Qiu, X. F. Chen, K. Y. Fu and Y. Q. Fan, The application of inorganic materials in uranium extraction from seawater-a review, *Sep. Purif. Technol.*, 2026, **382**(3), 135988, DOI: 10.1016/j.seppur.2025.135988.

14 D. Zhang, L. Fang, L. J. Liu, B. Zhao, B. W. Hu, S. J. Yu and X. K. Wang, Uranium extraction from seawater by novel materials: A review, *Sep. Purif. Technol.*, 2023, **320**, 124204, DOI: 10.1016/j.seppur.2023.124204.

15 X. Chang, P. Z. Hu, H. L. Liu, Z. X. Lv, J. Y. Yang, J. L. Wang, Z. Li, L. J. Qian and W. S. Wu, ZIF-8 modified graphene oxide/sodium alginate 3D elastic spheres for uranium trapping in seawater, *Desalination*, 2023, **549**, 116371, DOI: 10.1016/j.desal.2023.116371.

16 F. Wei, J. Z. Tong, X. Q. Liang, X. M. Wang, W. S. Wu, L. J. Qian and Z. Li, Glyphosine-Functionalized MIL-101(Cr)-NH2 for ultrafast uranium extraction from seawater, *Sep. Purif. Technol.*, 2025, **376**(1), 133887, DOI: 10.1016/j.seppur.2025.133887.

17 B. Ahmed, Z. Ahmad, A. Ihsan, M. A. Khan and T. Fazal, Biomaterials as promising biosorbents for efficient uranium extraction from seawater: A comprehensive review, *Sep. Purif. Technol.*, 2024, **338**, 126507, DOI: 10.1016/j.seppur.2024.126507.

18 Y. H. Yuan, Q. H. Yu, S. Yang, J. Wen, Z. H. Guo, X. L. Wang and N. Wang, Ultrafast Recovery of Uranium from Seawater by Bacillus velezensis Strain UUS-1 with Innate Anti-Biofouling Activity, *Adv. Sci.*, 2019, **6**(18), 1900961, DOI: 10.1002/advs.201900961.

19 Q. H. Yu, Y. H. Yuan, L. J. Feng, T. T. Feng, W. Y. Sun and N. Wang, Spidroin-Inspired, High-Strength, Loofah-Shaped Protein Fiber for Capturing Uranium from Seawater, *Angew. Chem., Int. Ed.*, 2020, **59**, 15997–16001, DOI: 10.1002/anie.202007383.

20 Z. H. Bai, Q. Liu, H. S. Zhang, J. Y. Liu, J. Yu and J. Wang, High efficiency biosorption of Uranium (VI) ions from solution by using hemp fibers functionalized with imidazole-4,5-dicarboxylic, *J. Mol. Liq.*, 2020, **297**, 111739, DOI: 10.1016/j.molliq.2019.111739.

21 S. W. Feng, L. J. Feng, M. Wang, Y. H. Yuan, Q. H. Yu, T. T. Feng, M. Cao, N. Wang and Q. Peng, Highly efficient extraction of uranium from seawater by natural marine crab carapace, *Chem. Eng. J.*, 2022, **430**(3), 133038, DOI: 10.1016/j.cej.2021.133038.

22 L. J. Guo, X. R. Lai, Z. X. Ma, L. Q. Peng, W. J. Long, W. H. Zhang and B. Shi, Lignin-based covalent organic polymers for highly efficient uranium extraction under highly acidic conditions, *Ind. Crop. Prod.*, 2024, **219**, 119119, DOI: 10.1016/j.indcrop.2024.119119.

23 J. H. Tang, J. L. Ma, G. J. Jiao, Y. H. Huang and R. C. Sun, Sulfomethylated lignin-intercalated layered double

hydroxide nanosheets for high-efficiency uranium extraction from seawater, *Sep. Purif. Technol.*, 2026, **382**(2), 135876, DOI: 10.1016/j.seppur.2025.135876.

24 T. S. Anirudhan, G. S. Lekshmi and F. Shainy, Synthesis and characterization of amidoxime modified chitosan/bentonite composite for the adsorptive removal and recovery of uranium from seawater, *J. Colloid Interface Sci.*, 2019, **534**, 248–261, DOI: 10.1016/j.jcis.2018.09.009.

25 A. Brewer, E. Chang, D. M. Park, T. Kou, Y. Li, L. N. Lammers and Y. Jiao, Recovery of rare earth elements from geothermal fluids through bacterial cell surface adsorption, *Environ. Sci. Technol.*, 2019, **53**, 7714–7723, DOI: 10.1021/acs.est.9b00301.

26 J. A. Francisco, C. F. Earhart and G. Georgiou, Transport And Anchoring Of Beta-Lactamase To The External Surface Of Escherichia-Coli, *Proc. Natl. Acad. Sci. U. S. A.*, 1992, **89**, 2713–2717, DOI: 10.1073/pnas.89.7.2713.

27 M. B. Nobari, M. R. Razavi, F. Hosseini, N. Amirmozafari and A. A. Sepahi, The Lpp-OmpA-BtaE fusion protein causes a protective immune response against *Brucella melitensis* in mice, *Sci. Rep.*, 2025, **15**, 27210, DOI: 10.1038/s41598-025-12059-7.

28 J. P. Lynch, L. Goers and C. F. Lesser, Emerging strategies for engineering *Escherichia coli* Nissle 1917-based therapeutics, *Trends Pharmacol. Sci.*, 2022, **43**, 772–786, DOI: 10.1016/j.tips.2022.02.002.

29 L. Zhou, M. Bosscher, C. Zhang, S. Oezcubukcu, L. Zhang, W. Zhang, C. J. Li, J. Liu, M. P. Jensen, L. Lai and C. He, A protein engineered to bind uranyl selectively and with femtomolar affinity, *Nat. Chem.*, 2014, **6**, 236–241, DOI: 10.1038/nchem.1856.

30 A. Brewer, A. Dohnalkova, V. Shutthanandan, L. Kovarik, E. Chang, A. M. Sawvel, H. E. Mason, D. Reed, C. Ye and W. F. Hynes, Microbe encapsulation for selective rare-earth recovery from electronic waste leachates, *Environ. Sci. Technol.*, 2019, **53**, 13888–13897, DOI: 10.1021/acs.est.9b04608.

31 S. Tiquia-Arashiro, X. Li, K. Pokhrel, A. Kassem, L. Abbas, O. Coutinho, D. Kasperek, H. Najaf and S. Opara, Applications of Fourier Transform-Infrared spectroscopy in microbial cell biology and environmental microbiology: advances, challenges, and future perspectives, *Front. Microbiol.*, 2023, **14**, 1304081, DOI: 10.3389/fmicb.2023.1304081.

32 A. D. Gupta, E. Kavitha, S. Singh and S. Karthikeyan, Toxicity mechanism of Cu^{2+} ion individually and in combination with Zn^{2+} ion in characterizing the molecular changes of *Staphylococcus aureus* studied using FTIR coupled with chemometric analysis, *J. Biol. Phys.*, 2020, **46**, 395–414, DOI: 10.1007/s10867-020-09560-7.

33 S. Correa-Garcia, M. Bermudez-Moretti, A. Travo, G. Deleris and I. Forfar, FTIR spectroscopic metabolome analysis of lyophilized and fresh *Saccharomyces cerevisiae* yeast cells, *Anal. Methods*, 2014, **6**, 1855–1861, DOI: 10.1039/c3ay42322k.

34 S. Gu and C. Q. Lan, Biosorption of heavy metal ions by green alga *Neochloris oleoabundans*: Effects of metal ion properties and cell wall structure, *J. Hazard. Mater.*, 2021, **418**, 126336, DOI: 10.1016/j.jhazmat.2021.126336.

35 G. Lu, A. J. Haes and T. Z. Forbes, Detection and identification of solids, surfaces, and solutions of uranium using vibrational spectroscopy, *Coord. Chem. Rev.*, 2018, **374**, 314–344, DOI: 10.1016/j.ccr.2018.07.010.

36 F. Askari, M. Zandi, P. Shokrolahi, M. H. Tabatabaei and E. Hajirasoliha, Reduction in protein absorption on ophthalmic lenses by PEGDA bulk modification of silicone acrylate-based formulation, *Prog. Biomater.*, 2019, **8**, 169–183, DOI: 10.1007/s40204-019-00119-x.

37 K. R. Mamaghani, S. M. Naghib, A. Zahedi and M. Mozafari, Synthesis and microstructural characterization of GelMa/PEGDA hybrid hydrogel containing graphene oxide for biomedical purposes, *Mater. Today: Proc.*, 2018, **5**, 15635–15644, DOI: 10.1016/j.matpr.2018.04.173.

38 F. Ahimou, C. J. P. Boonaert, Y. Adriaensen, P. Jacques, P. Thonart, M. Paquot and P. G. Rouxhet, XPS analysis of chemical functions at the surface of *Bacillus subtilis*, *J. Colloid Interface Sci.*, 2007, **309**, 49–55, DOI: 10.1016/j.jcis.2007.01.055.

39 Y. Ma, H. Zhong and Z. He, Cr(VI) reductase activity locates in the cytoplasm of *Aeribacillus pallidus* BK1, a novel Cr(VI)-reducing thermophile isolated from Tengchong geothermal region, China, *Chem. Eng. J.*, 2019, **371**, 524–534, DOI: 10.1016/j.cej.2019.04.085.

40 H. C. van der Mei, J. de Vries and H. J. Busscher, X-ray photoelectron spectroscopy for the study of microbial cell surfaces, *Surf. Sci. Rep.*, 2000, **39**, 3–24, DOI: 10.1016/S0167-5729(00)00003-0.

41 L. Yuan, H. Wei, X.-Y. Yang, W. Geng, B. W. Peterson, H. C. van der Mei and H. J. Busscher, *Escherichia coli* Colonization of Intestinal Epithelial Layers *In Vitro* in the Presence of Encapsulated *Bifidobacterium breve* for Its Protection against Gastrointestinal Fluids and Antibiotics, *ACS Appl. Mater. Interfaces*, 2021, **13**, 15973–15982, DOI: 10.1021/acsami.0c21790.

42 L. Zuo, W. Peng, Z. Xu, H. Guo and M. Luo, Selective adsorption of uranyl by glutamic acid-modified amidoxime fiber, *React. Funct. Polym.*, 2022, **179**, 105376, DOI: 10.1016/j.reactfunctpolym.2022.105376.

43 A. Froideval, M. Del Nero, R. Barillon, J. Hommet and G. Mignot, pH dependence of uranyl retention in a quartz/solution system: an XPS study, *J. Colloid Interface Sci.*, 2003, **266**, 221–235, DOI: 10.1016/s0021-9797(03)00528-9.

44 G. H. Yang, Y. Y. Zhang, Q. H. Zhu, X. Xia, N. Pan, C. Y. Ma, J. L. Liu, Y. Liu, Y. L. Qin, Q. D. Zhang, F. Q. Dong, J. Li and X. Q. Nie, Endeavoring a High Amidoxime Utilization Ratio and Adsorption Capacity for Uranium Extraction From Seawater: A Hydrogen Bonding Reconstruction Strategy, *Adv. Funct. Mater.*, 2025, **35**(22), 2425281, DOI: 10.1002/adfm.202425281.

45 J. Xiao, Y. Jing, X. Q. Wang, Y. Yao and Y. Z. Jia, Preconcentration of Uranium(VI) from Aqueous Solution by Amidoxime-Functionalized Microspheres Silica Material: Kinetics, Isotherm and Mechanism Study, *Chemistryselect*, 2018, **3**, 12346–12356, DOI: 10.1002/slct.201802472.

46 C. Y. Wang, M. Y. Xu, W. W. Wang and D. B. Hua, A Supramolecular Organic Framework-Mediated Electrochemical Strategy Achieves Highly Selective and Continuous Uranium Extraction, *Adv. Funct. Mater.*, 2024, **34**(41), 2402130, DOI: 10.1002/adfm.202402130.

47 F. X. Wang, C. Y. Li, W. T. Yang, W. X. Dou, C. Niu, Y. F. Liu and Q. H. Pan, Efficient Removal of U(VI) Using Functionalized Hollow Mesoporous Silica Nanospheres, *Chemistryselect*, 2019, **4**, 7396–7402, DOI: 10.1002/slct.201901411.

48 V. Bohl and A. Mogk, When the going gets tough, the tough get going-Novel bacterial AAA plus disaggregases provide extreme heat resistance, *Environ. Microbiol.*, 2024, 26, DOI: 10.1111/1462-2920.16677.

49 S. Goldberg, L. J. Criscenti, D. R. Turner, J. A. Davis and K. J. Cantrell, Adsorption - Desorption processes in subsurface reactive transport modeling, *Vadose Zone J.*, 2007, **6**, 407–435, DOI: 10.2136/vzj2006.0085.

50 A. Violante, Elucidating Mechanisms of Competitive Sorption at the Mineral/Water Interface, *Adv. Agron.*, 2013, **118**, 111–176, DOI: 10.1016/B978-0-12-405942-9.00003-7.

51 J. Liu, C. S. Zhao, G. Y. Yuan, Y. Dong, J. J. Yang, F. Z. Li, J. L. Liao, Y. Y. Yang and N. Liu, Adsorption of U(VI) on a chitosan/polyaniline composite in the presence of Ca/Mg-U(VI)-CO3 complexes, *Hydrometallurgy*, 2018, **175**, 300–311, DOI: 10.1016/j.hydromet.2017.12.013.

52 M. Jain, V. K. Garg and K. Kadirvelu, Cadmium(II) sorption and desorption in a fixed bed column using sunflower waste carbon calcium-alginate beads, *Bioresour. Technol.*, 2013, **129**, 242–248, DOI: 10.1016/j.biortech.2012.11.036.

53 M. Kapur and M. K. Mondal, Design and model parameters estimation for fixed-bed column adsorption of Cu(II) and Ni(II) ions using magnetized saw dust, *Desalination Water Treat.*, 2016, **57**, 12192–12203, DOI: 10.1080/19443994.2015.1049961.

54 S. K. Maiti, D. Bera, P. Chattopadhyay and L. Ray, Determination of Kinetic Parameters in the Biosorption of Cr (VI) on Immobilized Bacillus cereus M161 in a Continuous Packed Bed Column Reactor, *Appl. Biochem. Biotechnol.*, 2009, **159**, 488–504, DOI: 10.1007/s12010-008-8519-2.

55 Y. H. Yoon and J. H. Nelson, Application of Gas-Adsorption Kinetics 1. A Theoretical-Model For Respirator Cartridge Service Life, *Am. Ind. Hyg. Assoc. J.*, 1984, **45**, 509–516, DOI: 10.1080/15298668491400197.